

Routes to chaos and multiple time scale dynamics in broadband bandpass nonlinear delay electro-optic oscillators

Michael Peil,¹ Maxime Jacquot,¹ Yanne Koumou Chembo,¹ Laurent Larger,¹ and Thomas Erneux²

¹UMR CNRS FEMTO-ST 6174/Optics Department, University of Franche-Comté, 16 Route de Gray, 25030 Besançon Cedex, France

²Optique Non linéaire Théorique, Université Libre de Bruxelles, Campus Plaine CP 231, B-1050 Bruxelles, Belgium

(Received 19 October 2008; published 9 February 2009)

The response of a nonlinear optical oscillator subject to a delayed broadband bandpass filtering feedback is studied experimentally, numerically, and analytically. The oscillator loop is characterized by a high cutoff frequency with a response time $\tau \sim 10$ ps and by a low cutoff frequency with a response time $\theta \sim 1$ μ s. Moreover, the optoelectronic feedback also consists of a significant delay τ_D of the order of 100 ns. Depending on two key physical parameters, the loop gain β and the nonlinearity operating point Φ , a large variety of multiple time scale regimes are reported, including slow or fast periodic oscillations with different waveforms, regular or chaotic breathers, slow time envelope dynamics, complex and irregular self-pulsing, and fully developed chaos. Many of these regimes are exhibiting new features that are absent in the classical first-order scalar nonlinear delay differential equations (DDEs), which differ in the modeling by the low cutoff only. Nearly all kinds of solutions are recovered numerically by a new class of integro-DDE (iDDE) that take into account both the high and low cutoff frequencies of the feedback loop. For moderate feedback gain, asymptotic solutions are determined analytically by taking advantage of the relative values of the time constants τ , θ , and τ_D . We confirm the experimental observation of two distinct routes to oscillatory instabilities depending on the value of Φ . One route is reminiscent of the square wave oscillations of the classical first-order DDE, but the other route is quite different and allows richer wave forms. For higher feedback gain, these two distinct regimes merge leading to complex nonperiodic regimes that still need to be explored analytically and numerically. Finally, we investigate the theoretical limits of our iDDE model by experimentally exploring phenomena at extreme physical parameter setting, namely, high-frequency locking at strong feedback gain or pulse packages for very large delays. The large variety of oscillatory regimes of our broadband bandpass delay electro-optic oscillator is attractive for applications requiring rich optical pulse sources with different frequencies and/or wave forms (chaos-based communications, random number generation, chaos computing, and generation of stable multiple GHz frequency oscillations).

DOI: 10.1103/PhysRevE.79.026208

PACS number(s): 05.45.-a, 42.65.Sf

I. INTRODUCTION

Time-delayed feedbacks are responsible for diverse phenomena such as regenerative chatter between the machine tool and the workpiece [1], sudden changes in the qualitative dynamics of physiological processes [2,3], and laser pulsating outputs caused by optical feedback from a distant mirror [4]. A popular way to describe these effects is to formulate delay differential equations (DDEs) where the state of a variable at time t depends on its value at time $t - \tau_D$. However, DDEs are mathematically difficult to analyze and much of the recent understanding of their possible solutions essentially results from detailed computer simulations. This is particularly the case in optics where the effects of optical and optoelectronic feedback are studied in detail leading to systematic comparisons between experiments and theory. An important by-product of these research activities is the identification of specific classes of DDEs that show similar dynamical phenomena caused by the delay such as the stabilization of unstable steady states, square-wave oscillations, or fast quasiperiodic oscillations.

While developing broadband and high-speed optical intensity chaos generators for chaos communication [5–7], a particular electro-optical delay oscillator has been designed that revealed several new dynamical phenomena. Some of these observations may be qualitatively described using the standard scalar nonlinear DDE

$$\tau x' = -x + f[x(t - \tau_D)], \quad (1)$$

where a prime means differentiation with respect to time t , τ_D being the delay and τ being the linear relaxation time of the dependent variable. The nonlinear function $f(x)$ might practically, e.g., represent the negative feedback of a physiological control [8] [$f(x) = a(1 + x^n)^{-1}$], the reinjection of part of the output light into the input of a passive resonant optical cavity [9] [$f(x) = a[1 + 2b \cos(x - x_0)]$], or the delayed synchronization of two oscillators [10] [$f(x) = -a \sin(x)$]. Equation (1) has been studied in detail for its square-wave oscillations in the limit of large delays. However, some of our experimental observations cannot be captured by the solutions of Eq. (1) and they motivated the analysis of the following integro-DDE (iDDE)

$$\theta^{-1} \int_{t_0}^t x(\eta) d\eta + \tau x' = - \left(1 + \frac{\tau}{\theta} \right) x + f[x(t - \tau_D)], \quad (2)$$

where the integral term comes from the bandpass feature of the broadband amplifier commonly used in modern optical communications. In contrast to this, previous realizations of similar electro-optic oscillators [11–13] did not have the electronic filtering of a high-pass type (i.e., with a low-frequency cutoff). Here, the ratio between the integral time θ and the differential time τ corresponds to the ratio between

the high and the low cutoff frequencies characterizing the bandwidth of modern commercially available 10 Gb/s (or more) electronics for high speed optical links. In our setup, it may span almost six orders of magnitude and the delay τ_D can be widely adjusted between θ and τ . For short delays, the accessible range is limited by the minimal length of the fibers and electrical connectors required to close the optoelectronic feedback loop. This length corresponds to about one meter or less of optical fiber, leading to a delay of a few nanoseconds or even tenths of nanoseconds. On the other hand, very long delay of several tens of microseconds, corresponding to several kilometers of optical fiber, can be realized owing to the low absorption of modern fibers. In this paper, we concentrate on the case for which we have a nearly equally distributed logarithmic spacing of the different time constants, i.e.,

$$\theta \approx 10^3 \tau_D \approx 10^6 \tau. \quad (3)$$

Except for those studies devoted to specific oscillatory regimes [14–16], a systematic experimental and theoretical bifurcation analysis of an iDDE problem that depends on three distinct time constants is missing. Mathematically, the limit $\theta \rightarrow \infty$ of Eq. (2) leads to Eq. (1) but one needs to be cautious because this limit is singular [17]. As we will demonstrate, multiple time scale solutions are becoming the rule for sufficient feedback rate, providing new waveforms and new bifurcation mechanisms. None of our analyses are routine applications of singular perturbation technique, and they have been performed in detail for corresponding parameters and compared with the experimental results whenever it was possible, in particular for the low feedback gain conditions. For higher feedback gain, analytical studies are much more difficult, and thus experimental results are mainly confronted with numerics. Several numerical simulations and their analysis are reported, in order to additionally support the applicability of the iDDE model.

The article is organized as follows. In Sec. II, we describe the experimental setup as well as the instruments used to investigate the output of the optical oscillator. In Sec. III, we derive the iDDE model (2), and discuss the qualitative role of key physical parameters. We emphasize their practical tuning range and establish dimensionless dynamical equations. We also present the numerical tools that are used for the exploitation and discussion of the experimental data. Section IV reports the first periodic oscillations observed for low feedback gain. Using singular perturbation techniques, a detailed theoretical and numerical analysis is proposed, on the basis of the normalized iDDE. The higher feedback gain situations are then reported in Sec. V, mainly supported by numerical simulations due to the much more challenging dynamical complexity for an analytical approach. Section VI illustrates the extreme dynamics diversity with the same setup. The latter is elucidated using rf spectra bifurcation diagrams for complementary insight. We also present further interesting dynamical phenomena obtained for different particular settings of the physical parameters (influence of a varied high cutoff frequency or of a longer time delay). This section aims at showing some of the consequent open issues concerned by such iDDE dynamics and, thus, underlining the

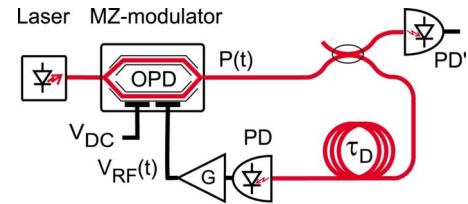


FIG. 1. (Color online) Experimental setup of the nonlinear electro-optic delay oscillator.

nonexhaustive content of the present article. We finally summarize our report, with discussions and conclusions in Sec. VII.

II. EXPERIMENTAL SETUP

The experimental setup is sketched in Fig. 1, showing the electro-optic nonlinear delay oscillator. Following the principle of Refs. [12,14], an optical nonlinear transformation of the electrical input of an integrated-optic electro-optic LiNbO₃ Mach-Zehnder (MZ) modulator, is performed by its two-wave interference modulation transfer function. The MZ is seeded by the light of a 1.55 μm DFB semiconductor laser whose power P_0 can be varied from 0 to around 10 mW. Note that the laser operates in an unmodulated continuous wave (CW) mode without any optical feedback. The nonlinearly modulated optical intensity at the MZ output is sent through an optical fiber which is mainly responsible for the time delay τ_D . Subsequently, the light enters the optoelectronic feedback path where intensity fluctuations are detected by a broadband amplified photodiode (PD) with 12 GHz bandwidth and $S=1.9$ V/mW conversion efficiency. This photodiode converts and filters the nonlinearly transformed optical signal back into the electrical domain. The electrical signal is then amplified by a broadband rf driver (18 dB gain, or amplitude amplification of $G=8$) which modulates via the electro-optic effect the optical path difference (OPD) of the MZ, thus closing the feedback loop of the nonlinear delay oscillator. Considering all the devices in the electronic path (i.e., optoelectronic detection, amplification, and electro-optic modulation of the OPD), the combined linear filtering process has a bandwidth of around 30 kHz–12 GHz, mainly limited by the amplified photodiodes. This broadband band-pass filtering is the dynamical phenomenon responsible for the integral and differential terms of the dynamics that appear in Eq. (2).

The light intensity dynamics of the MZ output can be analyzed at the free output of the 2×2 (50/50) fiber coupler. For monitoring, we either use a broadband unamplified dc-coupled photodiode PD' with 16 GHz bandwidth, or the amplified optical input of a 6 GHz real time digital oscilloscope, thus offering also a dc-coupled detection capability, but with a reduced bandwidth of 3.5 GHz. Low light intensities can be monitored best in time up to a maximum frequency of 3.5 GHz, whereas higher light intensities can also be detected with the broadband photodiode so that the recorded time series are only limited by the scope bandwidth, being 6 GHz. For the observation of faster frequencies up to the unamplified photodiode bandwidth (16 GHz), we also

have the possibility to connect the corresponding electrical output to a 22 GHz rf spectrum analyzer. Note that the actual intensity fluctuations might have much higher frequency components, due to the adiabatic nonlinear transformations performed by the interference effect. The OPD modulation via the electro-optic effect is indeed limited up to 12 GHz due to the electronic feedback path filtering. The adiabatic nonlinear MZ modulation transfer function might generate intensity fluctuations that exhibit the second or even the third harmonics of the OPD spectrum, depending on the OPD amplitude modulation. According to the amplifying capability of the electronic feedback, the rf driver can deliver up to 13 V peak-to-peak. Additionally considering that the rf electro-optic sensitivity of the MZ allows for a π -phase shift OPD for $V_{\pi,rf}=4.0$ V, an effective third order polynomial nonlinearity can be obtained via the utilized interference phenomenon. The measured signals are corresponding to a filtered—and thus slightly modified—version of the MZ output intensities, according to the combined filtering of the photodetector, and of the scope or rf spectrum analyzer.

III. BASIS FOR THEORY AND EXPERIMENT

A. Dynamical modeling of the setup

In order to investigate the behavior of our optical oscillator, we formulate a mathematical model of the form of Eq. (2). The main device responsible for the rich variety of dynamical responses is the broadband amplified photodetector. It is characterized by a high cutoff frequency with a response time τ and by a low cutoff frequency with the integral response time θ . The simplest description in the frequency domain for such a filter, corresponds to a second order band-pass filter with the following transfer function:

$$H(i\omega) = S \frac{i\omega\theta}{(1+i\omega\theta)(1+i\omega\tau)} = \frac{U(i\omega)}{P(i\omega)}. \quad (4)$$

In Eq. (4), $U(i\omega) \equiv V(i\omega)/G$ and $P(i\omega)$ are defined as the Fourier transform (FT) of the output voltage $u(t)$ and input optical power $p(t)$ of the photodiode. The optical power $p(t)$ is the one observed at the MZ output, but delayed in time by $\tau_D \equiv nL/c$, where L , n , and c are the length of the fiber generating the delay, its refractive index at the operating wavelength, and the speed of light in vacuum, respectively. Assuming a standard commercial telecom MZ, it is given by $p(t) = \alpha P_0 \cos^2[\pi v(t - \tau_D)/(2V_{\pi,rf}) + \Phi]$ where α accounts for the losses of the MZ and Φ is a static offset phase in the interference condition. The parameter Φ can be adjusted through a bias voltage on a couple of extra dc electrodes. Those electrodes thus have their own half wave voltage $V_{\pi,dc} \approx 4$ V, a value similar to $V_{\pi,rf}$. The voltage $v(t) = \text{FT}^{-1}[V(i\omega)]$ is the one applied on the rf electrodes of the MZ. It equals $Gu(t)$ assuming that the rf driver of gain G has a broader bandwidth than the one of the photodiode. Moreover, we assume that the bandwidth of the electro-optic effect exceeds that of the photodiode as well. It then implies that the filtered output of the photodiode is not filtered again by either the driver or by the MZ rf electrodes. Instead, the output signal is amplified with the gain G , and subsequently

converted into an optical phase difference in the MZ interferometer.

From Eq. (4), and using the conversion rules from the Fourier domain back to the time domain [$i\omega \rightarrow d/(dt)$ and $(i\omega)^{-1} \rightarrow \int dt$], we obtain

$$\begin{aligned} \tau v'(t)/G + \left(1 + \frac{\tau}{\theta}\right)v(t)/G + \frac{1}{\theta} \int_{t_0}^t v(s)/G ds \\ = \alpha P_0 S \cos^2 \left[\frac{\pi v(t - \tau_D)}{2V_{\pi,rf}} + \Phi \right]. \end{aligned} \quad (5)$$

In dimensionless form, this equation becomes

$$\tau x' + x + \theta^{-1} \int_0^t x ds = \beta \{ \cos^2[x(t - \tau_D) + \Phi] - \cos^2(\Phi) \}, \quad (6)$$

where we have neglected the small term $\tau/\theta \approx 2.45 \times 10^{-6}$. The arbitrary time t_0 has been chosen so that Eq. (6) admits a steady state for x ($x=0$). The dimensionless dependent variable $x \equiv \pi v/(2V_{\pi,rf})$ is proportional to the signal in the electronic feedback driving the MZ. Note that the observed quantity is not $x(t)$ but $f[x(t)]$, which is defined by

$$f(x) \equiv \beta \cos^2(x + \Phi). \quad (7)$$

It is the nonlinear transformation of x via the MZ modulation transfer function (output intensity of a two-wave interferometer). The normalized parameter $\beta \equiv \pi \alpha P_0 S G / (2V_{\pi,rf})$ measures the amplitude of the delayed feedback. It can be linearly increased by tuning the optical laser power P_0 , through laser diode injection current I_L . The feedback phase Φ is defined by $\Phi \equiv \pi V_{dc}/(2V_{\pi,dc})$ and is experimentally controlled via an external dc voltage V_{dc} applied across independent electrodes. Following the $f(x)$ nonlinearity, Φ gives rise to a π periodicity which can be scanned by V_{dc} over a $2V_{\pi,dc}$ range.

It is mathematically convenient to rewrite Eq. (6) as a system of two first-order differential equations. There are two different ways to do this and both derivations offer advantages for the analysis. The first way is to introduce the new variable $y \equiv \int_0^t x(s) ds$, leading to the following equations for y and x :

$$y' = x, \quad (8)$$

$$\tau x' = -x - \theta^{-1}y + \beta \{ \cos^2[x(t - \tau_D) + \Phi] - \cos^2(\Phi) \}. \quad (9)$$

A second way is to differentiate Eq. (6) with respect to t and formulate the following second-order DDE for x :

$$\tau x'' = -x' - \theta^{-1}x + \beta \{ \cos^2[x(t - \tau_D) + \Phi] \}'. \quad (10)$$

Introducing the new variable $z \equiv x'$, we then obtain

$$z' = z, \quad (11)$$

$$\tau z' = -z - \theta^{-1}x + \beta \{ \cos^2[x(t - \tau_D) + \Phi] \}'. \quad (12)$$

For clarity, the meaning and values of the fixed parameters are listed in Table I.

TABLE I. Physical and modeling parameters of the realized electro-optic nonlinear delay oscillator.

Parameter	Value	Meaning
τ_D	44.65 ns	delay
τ	13 ps	high frequency cutoff
θ	5.3 μ s	low frequency cutoff
P_0	0–10.5 mW	optical input
P_{sat}	≥ 10.5 mW	maximal input
α	0.082	optical losses parameter
S	1.9 V/mV	conversion efficiency of PD
G	8	power gain of amplifier
β	0–5.1	normalized feedback gain
$V_{\text{rf,max}}$	13.0 V	maximum rf voltage
$V_{\pi,\text{rf}}$	4.0 V	halfwave rf voltage
$V_{\pi,\text{dc}}$	4.1 V	halfwave dc voltage
Φ	$[-\pi/2, +\pi/2]$ rad	offset interference phase

In summary, the filtered optical feedback is described by the iDDE (6) which is equivalent to the system of two coupled first-order DDEs for either x and y [Eqs. (8) and (9)], or x and z [Eqs. (11) and (12)]. The formulation of our problem is based on the assumption of a second-order bandpass filtering. In practice, the bandpass process is more complex since the cutoff frequency stop band is measured to have an amplitude decay much faster than 20 dB/decade (as well as the start band at low frequency cutoff). A more accurate and complex description would, however, require several higher order derivatives as well as higher-order integrals.

B. Data analysis tools

We have mainly used three techniques for data analysis. A first rather global characterization of the dynamics corresponds to a bifurcation diagram–like representation, obtained for fixed values of all the parameters except Φ , which was finely tuned over its periodicity range, varying V_{dc} over a $2V_{\pi,\text{dc}}$ interval. For each value of Φ or, equivalently, V_{dc} , we have recorded long time series that allowed us to derive, for each dynamical regime, a probability distribution function (PDF) of the observed variable. In the model, this variable is related to the quantity $f[x(t)]$, the nonlinear transformation, but the obtained time series is inevitably a filtered version of $f[x(t)]$ according to the limited real time acquisition bandwidth of the instruments. A vertical cut of the bifurcation diagram versus V_{dc} thus consists of the color-scale encoded PDF, for a fixed dynamical regime, i.e., for fixed parameters (Φ , β , τ_D , etc.). Many such diagrams have been recorded for different values of the normalized feedback gain β from 1.3 to 5.1, obtained experimentally with laser diode currents I_L between 30 and 80 mA (optical input powers P_0 between 0 and 10.5 mW). For low feedback gains, we typically find low complexity dynamics, whereas higher gains usually lead to more complex nonlinear regimes, among which fully developed chaos can be experimentally achieved.

A second tool for characterization of the dynamics is the time series itself, from which we can determine the shape and the time scale of the waveform in dependence on the parameter Φ . The Φ values of the presented time series have been chosen so that they reveal the most important dynamical regimes among the vast variety of observable situations.

Finally a third technique, the direct rf spectral analysis (not obtained by calculation of the FFT of the time series, but measured with an electrical spectrum analyzer with a bandwidth of 22 GHz), is used to gain complementary insight into the dynamics in the spectral domain. It is particularly useful for higher complexity regimes, for which complex waveforms are obtained and analytical description is much more difficult. Additionally, it provides insight into the loss of information of the time domain measurements due to the limited bandwidth of the 6 GHz real time digital scope, which is about one half of the effective bandwidth of the optical intensity fluctuations. Due to the huge spectral range for the relevant frequencies, we recorded low-frequency spectra from 9 kHz to 100 MHz, and also broadband spectra from 7 MHz up to 19.4 GHz. This Fourier spectral analysis reveals the energy distribution in the frequency domain, thus indicating the actual characteristic frequencies of different dynamical regimes, sometimes enabling a discrimination between regimes of similar amplitudes but of different frequencies. For very complex solutions and multiple time scale waveforms, we also propose a wavelet analysis, which not only reveals the Fourier frequencies, but also their evolution in time along a very slow envelope.

IV. LOW FEEDBACK GAIN DYNAMICS

We analyze Eqs. (8) and (9) or Eqs. (11) and (12) both numerically and analytically and quantitatively compare experimental and theoretical observations whenever possible. The basic steady state solution $x=0$ is stable if $|\beta \sin(2\Phi)| < 1$ [16]. If $\beta < 1$, the trivial solution is always stable whatever the value of Φ is. If $\beta > 1$, a Hopf bifurcation is possible at $\beta = 1/|\sin(2\Phi)|$. If $\sin(2\Phi) > 0$, the Hopf bifurcation frequency is $\omega_+ \approx \pi/\tau_D$ implying the emergence of $2\tau_D$ -periodic limit-cycle oscillations. As β is further increased, we note numerically that this frequency remains constant although the waveform undergoes substantial changes. On the other hand, if $\sin(2\Phi) < 0$, the Hopf bifurcation frequency is $\omega_- \approx 2\pi/\tau_D$ and the bifurcation leads to τ_D -periodic oscillations. But as soon as β increases, we find the emergence of low-frequency oscillations with a period approximately 100 times larger than τ_D . This phenomenon is confirmed experimentally and is totally unexpected since it cannot be anticipated from the Hopf bifurcation analysis. We investigate both the low-frequency and square-wave oscillations in the Secs. IV B and IV D, respectively.

A. Experimental observations

For very low feedback gains of $\beta < 1$, there is nearly no feedback and the measured power at the MZ output is dc depending only on the parameter Φ , but not on the feedback. Gradually increasing Φ from negative values and detection

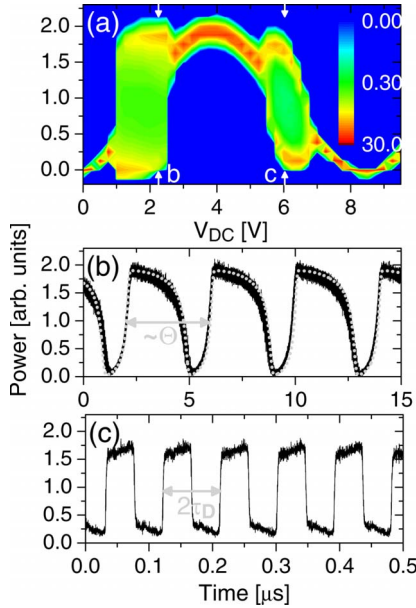


FIG. 2. (Color online) Dynamics for low feedback gain. (a) Probability distribution function of the intensity for $I_L=30$ mA ($\beta \approx 1.3$). Exemplary intensity time series are shown in panel (b) for $V_{dc}=2.25$ V and in (c) for $V_{dc}=6.00$ V ($\Phi=0.56$ and 0.64). The dotted gray line shows numerically obtained dynamics using Eq. (2).

with the dc-coupled PD' reveals the expected cosine square modulation provided by $f(x)$. In other words, the basic steady state is stable for all values of Φ .

As the feedback gain is increased by increasing the injected optical intensity, the linear stability analysis of the steady state predicts a change of stability for sufficiently high absolute value of the slope of the nonlinear function $f(x)$. This is shown in Fig. 2(a), where the PDF of the possible regimes is represented as a function of V_{dc} . The logarithmic color scale, which will be used in all our PDF plots, indicates the probability density in percent, normalized to the total number of events. It can be deduced from the figure that the Φ values corresponding to strong slopes of the $f(x)$ nonlinearity are no longer leading to stable steady states, but to widespread PDF indicating pulsating oscillatory regimes. Specifically, two distinct time-periodic regimes are observed in the bifurcation diagram of Fig. 2 [see the time traces in (b) and (c)]. In Fig. 2(b) a period of the order of θ is observed for positive slopes of the $f(x)$, whereas in Fig. 2(c) a period of the order of $2\tau_D$ occurs for the negative slope. The latter is clearly the regime predicted by the Hopf bifurcation at $\gamma = 1$ and is equivalent to the period-2 square-wave oscillations previously found for the Ikeda equation. Note that plateaus are not strictly constant due to the effect of θ (dc filtering out).

In Fig. 2(b), the numerical solution reproduces the low-frequency oscillations as it can be seen by the dashed gray line in Fig. 2(b). The good agreement between experiment and theory has been achieved for the parameters provided in Table I and with $\beta=1.3$ and $\Phi=-0.57$. Quantitative match is obtained by using $\theta=3.66$ μ s. This small difference might originate from the more complex filter profile than the one used in our model.

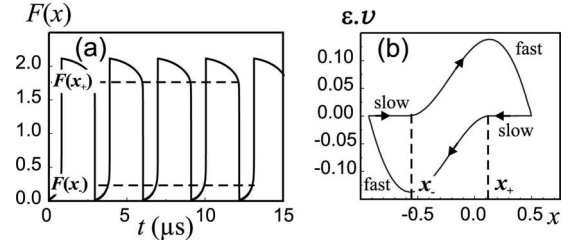


FIG. 3. Limit-cycle oscillations of the reduced (x, v) ordinary differential equations. The values of τ and θ are listed in Table I. The values of the control parameters are $\beta=1.3$ and $\Phi=-0.57$. The figure represents $F=1.632f(x)$, where the coefficient 1.632 has been determined by comparing experimental and numerical regimes. The points $x=x_{\pm}$ denotes the critical points where a fast transition layer occurs; (a) temporal waveform; (b) bird-shaped orbit in the phase plane $(x, \epsilon v)$. Fast and slow (where $v=x'$ is close to 0) parts of the orbit can be constructed analytically in the small- ϵ limit. They lead to the critical points x_{\pm} where the fast transition layers appear.

B. Low-frequency oscillations

The low-frequency oscillations observed experimentally and numerically for $\Phi=-1.57$ are not the result of the destabilizing effect of the delay, but it originates from a different bifurcation mechanism. We note that the period of the oscillations is in the μ s time range which corresponds to the time scale of θ . Introducing $s \equiv \theta^{-1}t$ and $v \equiv \theta z$ into Eqs. (11) and (12), we obtain

$$x' = v, \quad (13)$$

$$\epsilon v' = -v - x + \beta[\cos^2[x(s - \delta) + \Phi]]', \quad (14)$$

where differentiation is now with respect to s , ϵ , and δ being defined by

$$\epsilon \equiv \tau\theta^{-1} = 2.45 \times 10^{-6}, \quad \delta \equiv \tau_D\theta^{-1} = 8.43 \times 10^{-3}. \quad (15)$$

The low value of δ motivates to neglecting the delay in Eq. (14). The reduced equations then lead to the following system of two first-order ordinary differential equations:

$$x' = v, \quad (16)$$

$$\epsilon v' = -v - x + \beta[\cos^2(x + \Phi)]'. \quad (17)$$

The long-time numerical solution of Eqs. (16) and (17) is shown in Fig. 3(a). The oscillations are strongly pulsating with fast transition layers connecting slowly varying plateaus. The limit-cycle solution can be analyzed in the phase-plane and separate approximations for the slow and fast parts of the orbit can be determined analytically in the limit of ϵ small [see Fig. 3(b)]. We omit all details of the analysis and only concentrate on the main results. In first approximation, the slowly varying plateaus of the envelope satisfy Eq. (17) with $\epsilon=0$ given by

$$v = -x + \beta[\cos^2(x + \Phi)]'. \quad (18)$$

After differentiating the last term in Eq. (18) and using Eq. (16), Eq. (18) can be rewritten as

$$v = -\frac{x}{1 + \beta \sin(2x + 2\Phi)}. \quad (19)$$

This approximation fails as soon as the denominator in Eq. (19) approaches zero. The critical points $x=x_{\pm}$ satisfying the condition

$$\beta \sin(2x + 2\Phi) = -1, \quad (20)$$

are the points where the limit-cycle undergoes the fast transition layers. They are given by

$$x_+ = -\frac{1}{2} \arcsin(\beta^{-1}) - \Phi, \quad (21)$$

$$x_- = \frac{1}{2}[-\pi + \arcsin(\beta^{-1})] - \Phi. \quad (22)$$

Using the values of β and Φ , we determine $x_+ \approx 0.13$ and $x_- \approx -0.56$. These critical points are necessary for observing the bird-shaped limit cycle in Fig. 3(b). Note that Eq. (20) for x_{\pm} contains the previous observation that the low-frequency oscillations only appear if $\beta \sin(2\Phi) < -1$, which is the case [$\beta \sin(2\Phi) \approx -1.18$]. If we now compare the oscillations shown in Fig. 3(a) with the experimental oscillations shown in Fig. 2, we note similar amplitudes for the plateaus but smoother transition layers in the case of the experimental observations. We attribute this difference to the effect of the actual presence of the small delay during the fast transitions layers. This effect is ignored in the leading order problem (16) and (17), according to the adopted hypothesis.

C. Stability of the low-frequency oscillations

The rapid bursting oscillations observed numerically and experimentally motivates a stability analysis of the slowly varying envelope. Recall that the leading approximation of the slowly varying plateaus satisfies Eq. (17) with $\varepsilon = \delta = 0$. With Eq. (16) but keeping the delay δ , Eq. (17) now reduces to

$$x' + x = \beta \{\cos^2[x(s - \delta) + \Phi]\}'. \quad (23)$$

We analyze this equation by a multitime scale analysis where $\zeta \equiv \delta^{-1} s$ is the fast time and s is the previously defined slow time of the slowly varying plateaus. We summarize the main results. The leading approximation $x = x_0(\zeta, s)$ satisfies the following equation:

$$x_0 = \beta \cos^2[x_0(\zeta - 1) + \Phi] + F, \quad (24)$$

where F is the constant of integration. The expression (24) provides the successive maxima and minima, $x_0 = x_{0n}$, of a square-wave-like solution. The extrema x_{0n} satisfies the following equation for a map:

$$x_{0n} = \beta \cos^2(x_{0n-1} + \Phi) + F. \quad (25)$$

Note that we have obtained Eq. (25) by integrating Eq. (23) with respect to the fast time ζ . Consequently, we need to assume that the constant of integration F is a function of the slow time s . In order to obtain an equation for F , we need to

investigate the higher-order problem for $x = x_1$ and apply a solvability condition. This condition is

$$\frac{dF}{ds} = -\lim_{\zeta \rightarrow \infty} \frac{1}{\zeta} \int_0^{\zeta} x_0(s, \xi) d\xi. \quad (26)$$

A period-1 fixed point of Eq. (25) corresponds to $x_n = x_{n-1} = x^*$. From Eqs. (25) and (26), we find

$$x^* = \beta \cos^2(x^* + \Phi) + F, \quad (27)$$

$$\frac{dF}{ds} = -x^*. \quad (28)$$

Differentiating Eq. (27) with respect to s and using Eq. (28), we correctly obtain Eq. (18) describing the slowly varying plateaus. Thus, the period-1 fixed point solution correctly match the slowly varying envelope of the rapid oscillations. In order to determine if rapidly varying oscillations are possible, we need to determine if a period-2 fixed point is possible. We consider $x = x^*$ as our reference solution and keep F constant. F is defined by means of Eq. (27), i.e.,

$$F = x^* - \beta \cos^2(x^* + \Phi). \quad (29)$$

From Eq. (25), we determine the following linearized equation for $x = x^*$:

$$u_n = -\beta \sin(2x^* + 2\Phi) u_{n-1}, \quad (30)$$

where $u_n \equiv x_n - x^*$ is defined as the small perturbation. Seeking then a solution of the form $u_n = r^n$, the characteristic equation for r is

$$r = -\beta \sin(2x^* + 2\Phi). \quad (31)$$

The solution $x = x^*$ (F constant) is stable if $|r| < 1$, i.e., when $|\beta \sin(2x^* + 2\Phi)| < 1$. The critical condition $r = 1$ marks a saddle-point, i.e., if $\beta \sin(2x^* + 2\Phi) = -1$. This condition exactly matches the condition (20) for the onset of the fast transition layers. On the other hand, the critical condition $r = -1$ marks a Hopf bifurcation point, i.e., if

$$\beta \sin(2x^* + 2\Phi) = 1. \quad (32)$$

The solutions of Eq. (32) are

$$x_{H+} = \frac{1}{2} \arcsin(1/\beta) - \Phi, \quad (33)$$

$$x_{H-} = \frac{1}{2}[-\pi - \arcsin(1/\beta)] - \Phi. \quad (34)$$

For $\Phi = -\pi/10$ and $\beta = 2.5$, we find $x_{H+} = 0.5199$ and $x_{H-} = -1.462$. Later on in Sec. V, we will also demonstrate the occurrence of this analytically derived behavior in the experiment. Figure 4 show the bifurcation diagram of the stable solutions of the map (25). To complete the analysis of the bursting oscillations, we need to take into account the slow evolution of F described by Eq. (26) which has been ignored here for simplicity.

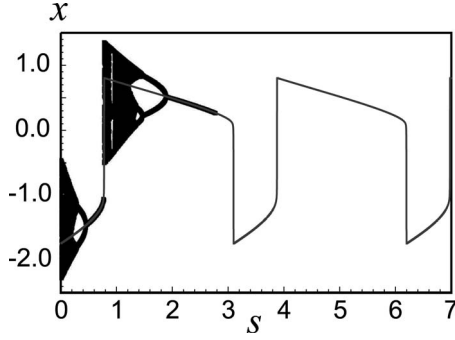


FIG. 4. The bifurcation diagram of the extrema of the rapid oscillations overlap the slowly varying envelope. $\Phi = -\pi/10$ and $\beta = 2.5$.

D. Square-wave oscillations

We first introduce the delay time $s \equiv t/\tau_D$ as our basic reference time. Together with $u \equiv y\tau_D^{-1}$, Eqs. (8) and (9) become

$$u' = x, \quad (35)$$

$$\varepsilon_1 x' = -x - \delta u + \beta \{ \cos^2[x(s-1) + \Phi] - \cos^2(\Phi) \}, \quad (36)$$

where prime now means differentiation with respect to s . δ is defined in Eq. (15) and the new parameter ε_1 is given by

$$\varepsilon_1 \equiv \tau/\tau_D \approx 2.9 \times 10^{-4}. \quad (37)$$

A typical long time solution of Eqs. (35) and (36) has been determined numerically and is shown in Fig. 5. x and u exhibit square-wave and sawtooth oscillations, respectively. In the limit $\varepsilon_1 \rightarrow 0$, Eqs. (35) and (36) reduce to the following problem for u and x :

$$u' = x, \quad (38)$$

$$0 = -x - \delta u + \beta \{ \cos^2[x(s-1) + \Phi] - \cos^2(\Phi) \}. \quad (39)$$

Equations (38) and (39) are describing a map in x combined with a differential equation in u . Starting from arbitrary initial conditions $u(0) = u_0$ and $x = x_0$ ($1 < s < 0$), we have numerically found that the solution of Eqs. (38) and (39) slowly evolves (on a long δ^{-1} time scale) towards a bounded square-wave solution for x . The plateaus of the square wave are almost constants and the size of the transition layers is $O(\delta)$ small. We wish to determine the square-wave two-

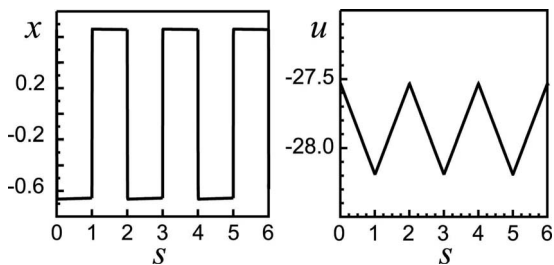


FIG. 5. Long time solution of the full iDDE problem for $\Phi = 0.57$, $\beta = 1.5$, $\varepsilon_1 = 2.9 \times 10^{-4}$, and $\delta = 8.43 \times 10^{-3}$.

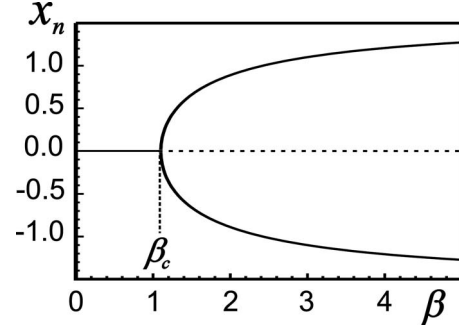


FIG. 6. Bifurcation diagram of the square-wave oscillations for $\beta = 0.57$. $x_n = x_{n0}$ is determined from a map derived in the double limit $\varepsilon_1 \rightarrow 0$ and $\delta \rightarrow 0$. The bifurcation point is located at $\beta_c = 1/\sin(2\Phi) = 1.1$. At $\beta = 1.5$, the extrema are located at $x = \pm 0.66$ which matches the values found numerically from solving the original iDDEs.

periodic solution in the limit $\delta \rightarrow 0$. To this end, we seek a solution of the form

$$u_n = \delta^{-1} u_{n0}(s) + u_{n1}(s) + \dots, \quad (40)$$

$$x_n = x_{n0}(s) + \delta x_{n1}(s) + \dots, \quad (41)$$

where the subscript n refers to the time interval $n < s < n+1$ ($n=0, 1, 2, \dots$). The δ^{-1} scaling in Eq. (40) is motivated by the fact that u needs to be $O(\delta^{-1})$ in order to remain in Eq. (39) as $\delta \rightarrow 0$. Introducing Eqs. (40) and (41) into Eqs. (38) and (39), and equating to zero the coefficients of each power of δ leads to a sequence of simpler problems for the unknown functions in Eqs. (40) and (41). From Eq. (38), we find that

$$u'_{n0} = 0 \text{ and } u'_{n1} = x_{n0} \quad (42)$$

while from Eq. (39), we obtain that

$$-x_{n0} - u_{n0} + \beta \{ \cos^2(x_{n-1,0} + \Phi) - \cos^2(\Phi) \} = 0. \quad (43)$$

Equation (42) for u_{n0} implies that u_{n0} is a constant for all n . But Eq. (43) then implies that x_{n0} is also constant. Integrating Eq. (42) and taking into account the continuity of the solution at each $s = n$, gives

$$u_{01} = x_{00}s,$$

$$u_{11} = x_{00} + x_{10}(s-1),$$

$$u_{n1} = x_{00} + x_{10} + \dots + x_{n-1,0} + x_{n0}(s-n) \quad (44)$$

($n < s < n+1$). A period-2 square-wave solution satisfies the conditions

$$u_{11}(2) = u_{01}(0) \text{ and } x_{20} = x_{00}. \quad (45)$$

Using Eq. (44), the first condition requires

$$x_{00} + x_{10} = 0, \quad (46)$$

which is illustrated by the antisymmetric extrema for the stable limit cycle shown in Fig. 6. The second condition implies, using Eq. (43), that

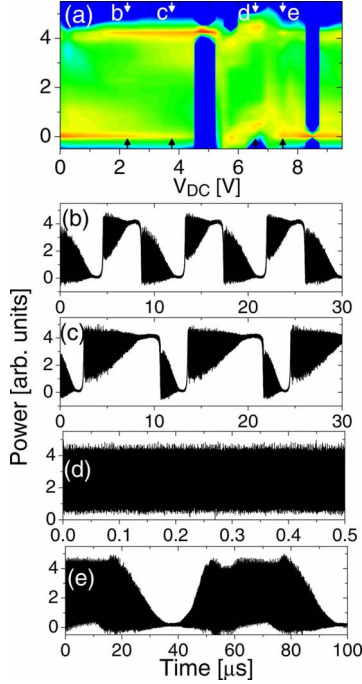


FIG. 7. (Color online) Dynamics for moderate feedback gain. (a) Probability distribution [color scaling, same as in Fig. 2(a)] of the intensity, for $I_L=45$ mA ($\beta \approx 2.4$). Characteristic intensity time series are shown in (b) for $V_{dc}=2.25$ V, (c) $V_{dc}=3.75$ V, (d) $V_{dc}=6.50$ V, and (e) $V_{dc}=7.50$ V.

$$-x_{10} - u_{n0} + \beta[\cos^2(x_{00} + \Phi) - \cos^2(\Phi)] = 0, \quad (47)$$

$$-x_{00} - u_{n0} + \beta[\cos^2(x_{10} + \Phi) - \cos^2(\Phi)] = 0. \quad (48)$$

Subtracting these two equations and using Eq. (46), we eliminate u_{n0} and x_{10} and obtain the following equation for x_{00} only:

$$2x_{00} + \beta[\cos^2(x_{00} + \Phi) - \cos^2(-x_{00} + \Phi)] = 0. \quad (49)$$

Using trigonometric identities, $x_{00}=x_{00}(\beta)$ is given by (in implicit form)

$$\beta = \frac{2x_{00}}{\sin(2\Phi)\sin(2x_{00})}. \quad (50)$$

This solution is shown in Fig. 6 together with $x_{10}=-x_{00}$. A numerical study of Eqs. (38) and (39) indicates that the period-2 square-wave solution remains stable until $\beta=2.1$. Above this value, the two plateaus of the period-2 solution start to break allowing more fast transition layers.

V. MODERATE TO HIGH GAIN DYNAMICS

A. First interplay of slow and fast time scales

Figure 7 shows a similar experimentally obtained bifurcation diagram as in Fig. 2, but for a larger feedback rate. We note that the Φ range for which a stable steady state can be obtained is now limited to the maxima of $f(x)$ where the slope is still sufficiently low to counterbalance the feedback gain.

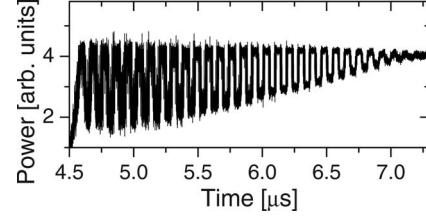


FIG. 8. Zoom into the chaotic breathers dynamics presented in Fig. 7(b).

Due to the higher gain, the various solutions depending on Φ now give rise to a more complex structure, in which the different intrinsic oscillator time scales start to be involved simultaneously. Analytical approaches are thus becoming more difficult from that level of the feedback gain. Therefore, we plan to compare all our observations with numerical simulations of Eq. (2). Four typical time traces are shown in Figs. 7(b)–7(e). Figures 7(b)–7(d) corresponds to two bifurcations of the two previously described oscillatory regimes. Figure 7(e) is the most complex regime observed for moderate feedback, it can, however, be reproduced by simulation of our iDDE model with excellent qualitative agreement with the experiment.

Figures 7(b) and 7(c) are observed for negative values of Φ [i.e., positive slope of $f(x)$]. It is indeed corresponding to the bifurcated state of the low-frequency oscillations, as predicted analytically in the previous section and shown in Fig. 4. Here, the low-frequency dynamics introduces a sweeping of the fast dynamical states along a standard Ikeda-like bifurcation diagram with a period doubling route to chaos. The sweeping is, however, definitely not externally imposed by varying a bifurcation parameter, but it is self-generated by the iDDE dynamics, with a scanning period related to the slow time scale θ . The fast bursting oscillations are observed with one slow period of the envelop. The experimental fast bursting oscillations overlapping the upper slow envelope are represented in Fig. 8, a magnification of Fig. 7(b). They first consist of large amplitude oscillations (chaotic part of the swept Ikeda-like bifurcation diagram) with an irregular internal structure exhibiting fast fluctuations of the order of the characteristic time τ . As the envelope amplitude decreases, the dynamics becomes more and more regular, and are almost periodic in a square wave fashion. The periodicity is then twice the delay τ_D as expected from our analysis. When the envelope dies out, the amplitude goes to zero and the dc level switches, in the same way as was analytically shown for the fast transition layer of the bird limit-cycle initiating a new bursting activity. This sequence of high and low fast oscillations appear periodically. After careful numerical investigations (suppression of very long transients), we found this slow-fast oscillatory regime from the numerical integration of the iDDE model. Such regimes have been called earlier chaotic breathers in Ref. [16].

Similar behaviors have been obtained experimentally for deviations of the feedback gain β of about 10%, and over a continuous range of the bias voltage V_{dc} between 0–4.1 V, which corresponds to an offset phase interval of $-\pi/2 < \Phi < 0$ (this range covers the segment of the nonlinear function with a positive slope). Depending on the level of the feed-

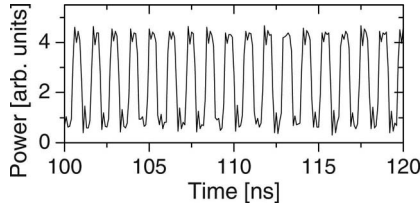


FIG. 9. Zoom into the nearly periodic dynamics shown in Fig. 7(d).

back gain β , a full or a partial Ikeda-like bifurcation diagram is observed, from the steady state to chaotic oscillations (for the higher β values of the 10% variation range), or from the steady state to the first period doubling regimes (for the lowest β values). The influence of the parameter Φ controls the asymmetry between the lower and the upper envelope of the Ikeda-like bifurcation diagram, and it affects the pseudoperiodicity of the two bursting events during a complete slow period. These effects can be seen from the time series presented in panel Fig. 7(c) compared with the ones in panel (b), or from Fig. 7(a) through the thickness of the upper and lower horizontal red line in the left part of the bifurcation diagram ($V_{dc} \in [0, 4.1]$).

We next concentrate on the regime in Fig. 7(d) related to positive values of Φ [i.e., negative slope of $f(x)$]. This Φ -parameter range corresponds to the $2\tau_D$ -periodic square-wave oscillations in the previous section. With the slightly higher feedback imposed in this section, they are suddenly changing into rapid oscillations with a period much shorter than $2\tau_D$. Small noiselike amplitude variations are also present. To gain insight into the behavior on the fast time scales, a zoom is shown in Fig. 9. The figure exhibits a constant envelope amplitude and the slow time scale θ does not appear. The fine structure is a nearly periodic and symmetric, with a period related to about 14 times the fast time scale τ , and exactly $1/79$ times τ_D . This surprising rational correspondence of the characteristic frequency is most probably the signature of a harmonic resonance between the inverse of the delay τ_D and the fast time scale τ . Similar regimes were described in the literature for Ikeda DDE, also called higher harmonic synchronization [21]. They are observed here in a robust way with respect to small parameter changes in β and Φ . The range of Φ for which this regime is observed approximatively corresponds to a local nonlinear function $f(x)$ with negative slope, and concave curvature.

The third characteristic regime of the bifurcation diagram in Fig. 7(a) is presented by the time series depicted in Fig. 7(e). This regime is probably one of the richest in terms of diversity and relevant time scales. It is obtained for a negative slope range of the nonlinear function $f(x)$, with either positive [convex profile of $f(x)$] or negative (concave profile) sign of the second derivative of $f(x)$. It is, however, best pronounced experimentally for convex curvature (close to a minimum) since, with a concave curvature (close to a maximum), its observation requires more critical parameter tuning. We analyze this feature as follows: Eq. (5) is indeed invariant with respect to the symmetry $x \rightarrow (\pi - x)$, because of the antisymmetry of the nonlinear function, and because the feedback is not dc preserving. Thus $(\pi - x)$ becomes

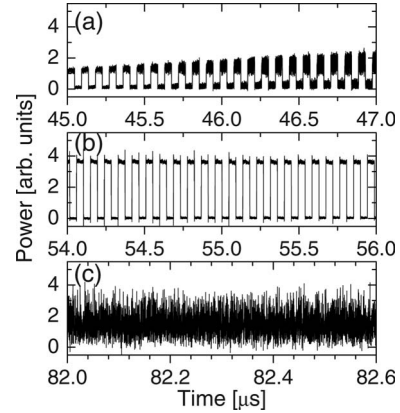


FIG. 10. Zooms into three different dynamical events occurring during the temporal evolution of the single envelope breathers dynamics of Fig. 7(e).

equivalent to $(-x)$ on the left-hand side: this gives a reason why we observe this regime (and also others for different feedback levels) on both sides of the antisymmetry point of $f(x)$, i.e., the inflection point, where the second derivative vanishes. However, symmetry is experimentally broken by the noise level within the feedback loop, which is higher close to a maximum of $f(x)$ (higher shot noise in the photodiode). This observation seems to be reasonably correlated with the greater experimental difficulties to reach the regime when operating close to a maximum, since noise contributes more significantly in lowering the deterministic impact on the actually observed regime.

The detailed evolution of the fast structure along the slow envelope of the regime in Fig. 7(e) is analyzed by using the magnified time series in Fig. 10, and with the help of the wavelet transform reported in Fig. 11. The global shape of this regime qualitatively recalls the breathers dynamics shown in Fig. 7(b) and reported in Ref. [16], but without the

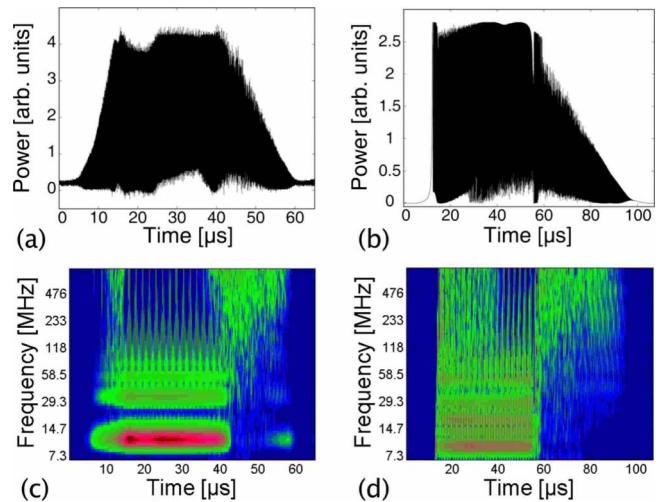


FIG. 11. (Color online) Time traces (upper) and wavelet analysis (lower). (a), (c) For the experimental time trace in Fig. 7(e) and (b), (d) for a time trace obtained numerically from the model in Eq. (2). The normalized parameters considered for the simulation are $\beta=2.8$ and $\Phi=2.04$, and the other parameters are listed in Table I.

switching events between the two different upper and lower envelopes. By contrast, this dynamical regime exhibits consecutive but similar envelop events, each starting from nearly zero amplitude and mean level, followed by fast oscillations of increasing amplitudes. This “mean” amplitude varies on a slow time scale (of the order of θ) until the amplitude slowly decays before the next event starts. The structure and the shape of the envelope of the rising and falling edges look similar and almost symmetric. A zoom into the rising edge is presented in Fig. 10(a) which gives insight into the dynamics on the faster time scales. We find that the rising edge starts from zero with a continuously growing amplitude squarelike waveform, with a $2\tau_D$ period. As the dynamics evolves towards higher amplitudes, the upper and lower plateaus of the square waveform become more and more noisy. This scenario resembles the period doubling cascade and inverse cascade of standard scalar delay equations when the feedback gain is used as a bifurcation parameter (see, e.g., Refs. [12,18]). As already discussed for the dynamics in Figs. 7(b) and 7(c), it is as if the slow integration time θ induces a sweeping of a fast Ikeda-like bifurcation diagram. However, no parameter of the bandpass oscillator is varied in time, and thus the slowly varying fast dynamics should be considered as a full dynamical regime. We expect that under such fixed parameter settings, the broadband bandpass dynamics experiences slow time scale instabilities, which might be related to a competition between the slow characteristic time θ and the transient characteristic time of the equivalent low pass delay dynamics. The latter is indeed typically in the order of several 10 or 100 times the delay and is comparable to θ .

After this starting event of the envelope until large amplitude values of 4 (in the vertical arbitrary unit of the time traces), the maximum amplitude of the fast oscillations experiences a small but abrupt change at $t \approx 52 \mu\text{s}$, from values slightly above down to slightly below 4 a.u. This abrupt change corresponds to the switching at faster time scales of the previous noisy fluctuations plateaus, to nearly square waves and large amplitude $2\tau_D$ oscillations as shown in Fig. 10(b). This square wave oscillation is maintained over several tens of microseconds with a nearly constant upper plateau level, and a very slowly increasing lower plateau level, until $t \approx 78 \mu\text{s}$. Then, the oscillation changes again to fully developed large amplitude broadband chaos. After this transition, the dynamics admits the complete available dynamical bandwidth, from the low frequency cutoff related to θ , up to the high-frequency cutoff related to τ . This is illustrated by the 600 ns zoom at $t \approx 78 \mu\text{s}$ given in Fig. 10(c). The transition to chaos is linked to an evolving decrease of the average rf power of the oscillator. Accordingly, the amplitude of the dynamics then continuously decreases to almost zero. At the very small amplitude of the fast chaotic oscillations, the envelope recovers some τ_D periodic structure before completely vanishing down to zero, similarly to the oscillations shown in Fig. 8. This “off state” lasts for a few microseconds (of the order of θ again), until a new envelope starts.

Analytical investigations of this complex regime is challenging. However, numerical (rather time consuming) investigations allowed us to clearly link this experimental observation to the iDDE model established theoretically for our setup. The agreement between experiment and numerical

simulations is particularly relevant for further investigations of the time traces through a more detailed time-frequency wavelet analysis, as depicted in Figs. 11(b) and 11(d). This complementary analysis reveals the diversity of the fast oscillations observed along the whole duration of the slow envelope, and the chronology of their occurrence. The wavelet analysis involves a vertical logarithmic frequency scaling which provides visual insight into the spectral evolution of the dynamics over the full duration of the slow envelope. We refer to the Appendix for a brief description of the continuous wavelet transform.

The numerical simulations of this regime is very demanding because the dynamics admits all characteristic time scales, spanning more than six orders of magnitude. Numerical simulations with the actual experimental time parameter values were only possible when particular care in the calculation procedure was taken (see the Appendix), because of memory overflow. The numerical results qualitatively confirm the validity of the iDDE model. In Fig. 11 we compare experimental [(a) and (c)] and numerical [(b) and (d)] results: in the first two third of the slow envelope, we observe nearly periodic square waves with intermediate frequencies related to the inverse of twice the delay ($1/\tau_D$), whereas the last third of the slow envelope reveals a broadband chaoticlike spectrum, spreading up to high frequencies of the order of $1/\tau$. Only the starting edge of the envelope differs between numerics and experiments. We note a continuously increase of the envelope amplitude in the experiment, whereas the numerical solution is more abruptly starting with large amplitude oscillations. Abrupt large amplitude oscillations are observed experimentally in Figs. 7(b) and 7(c), Fig. 8, and have been reported for breathers in Ref. [16]. However, our simulations were unable to reproduce the smooth start of the envelope amplitude [as reported in Figs. 7(e) and 11(a)].

B. Unstable steady states

Further increasing the feedback gain fully destabilizes the dynamics for any value of the offset phase Φ . The stable fixed points previously located at the extrema of the nonlinear function at around 4.7 and 8.5 V, still present for $I_L = 45 \text{ mA}$ [see Fig. 7(a)], disappear as it can be seen in the bifurcation diagram for $I_L = 50 \text{ mA}$ shown in Fig. 12(a). For this slightly higher feedback gain, we do not find important qualitative changes by contrast to what we have observed for a small increase of β in the regimes of lower feedback gains.

Nevertheless, one additional dynamical phenomena arises which is illustrated by the time series in Fig. 12(b) and its zoom shown in panel (c). The dynamics in this regime resembles the one already described in Figs. 7(c) and 9, because it exhibits a similar period for the fast dynamics. However, the higher gain condition allows for a destabilization of the constant amplitude of the oscillation observed previously. Here a second amplitude level arises and leads to a slower time scale connected with a periodic square wave amplitude modulation (AM) of the fast oscillations. The AM time scale is of the order of the delay τ_D , while the slow characteristic time θ does not seem to play any role. Similar behaviors have been reported in the literature on delay dynamics: one

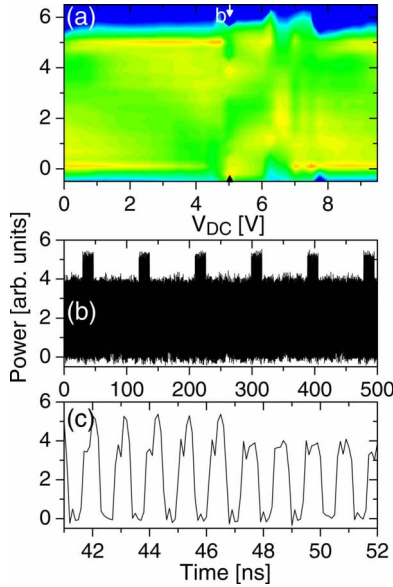


FIG. 12. (Color online) (a) Probability distribution [color scaling, same as in Fig. 2(a)] of the intensity for $I_L=50$ mA ($\beta \approx 2.8$). (b) Possible isomeric state of the intensity time series for $V_{dc}=5.00$ V. (c) Zoom into (a).

case focuses on the low pass feedback scheme (Ikeda or Mackey-Glass) [19], and another case has been described very recently [20] for the bandpass scheme, but with a narrow band character (a setup intended for generation of high spectral purity microwave oscillations).

In the first case, it is well known that successive higher-harmonic bifurcations can occur for sufficiently large delay [21], and lead to multistable periodic solutions known as “isomers” [19]. The time series presented in Fig. 12(b) reveals both properties, i.e., a very high harmonic (79) of the fundamental $P2$ oscillation and an additional AM pattern repeating each $2\tau_D$. Due to the long delay in our setup, we have observed that the AM pattern can vary substantially even for small changes of the key parameters, giving experimental indication for multistability.

In the second case [20], the delay dynamics involves a very narrow bandpass filter in addition to a very long delay line (several kilometers). It was then demonstrated that the desired oscillation [22,23], can exhibit a secondary bifurcation of its amplitude through an increase of the feedback gain. It was shown that the instability mechanism observed in that bandpass scheme, was of the same kind than that for the low pass case, but from the envelope dynamics rather from the microwave oscillation.

C. Influence of the phase for the high feedback

The possible regimes for high feedback gain are shown in the bifurcation diagram of Fig. 13. The two distinct responses depending on Φ have disappeared for a fully developed chaotic dynamics. These regimes are of particular interest for chaos communications [6,7]. In this regime the dynamics typically feature a flat and broadband rf spectrum with an all-time scale chaotic time trace (almost noise-like),

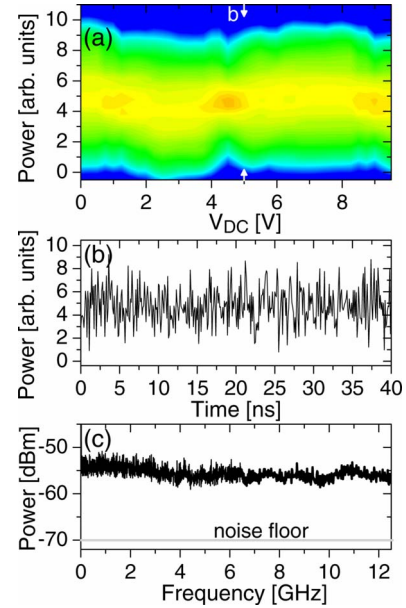


FIG. 13. (Color online) Dynamics for high feedback gain. (a) Probability distribution of the intensity for $I_L=70$ mA ($\beta \approx 4.3$). (b) Intensity time series for $V_{dc}=6.50$ V. (c) Corresponding rf spectra.

continuously spanning a very broad temporal scale from the slow (θ), via the intermediate (τ_D), to the fast (τ) characteristic times. The large amplitude waveform is a signature of a strong nonlinear regime. Practically this means that the amplitude at the input of the nonlinear function $f(x)$ is able to scan much more than one extremum, and even up to three according to the voltage swing capability of our rf driver, compared to the $V_{\pi,rf}$. The strong nonlinear delay feedback is also known to allow for a nearly Gaussian PDF [24,25] in the standard scalar differential delay dynamics. Performing a vertical cut in Fig. 13 for almost any value of V_{dc} , we find a vertical color distribution of the PDF corresponding to a bell-like shape which can either be perfectly symmetric, or slightly tilted towards higher or lower power levels depending on Φ .

VI. COMPLEMENTARY EXPERIMENTS

A. rf spectral overview over the dynamics

Figure 14 reveals the spectral signature of the previously described bifurcation diagrams of Figs. 2(a), 7(a), 12(a), and 13(a). It highlights the frequency range typically associated to the inverse of the delay time $\tau_D \approx 45$ ns, so that $\nu_{P2} = 1/(2\tau_D) \approx 11$ MHz. For the low gain condition in Fig. 14(a), the square wavelike oscillation is confirmed by the presence of the frequency ν_{P2} and its odd harmonics. This holds for the parameter Φ region which corresponds to the strongest negative slope at around $V_{dc}=6.25$ V (the decreasing linear part of the \cos^2 nonlinearity). Some spurious even harmonic are also present in the strong positive slope region close to $V_{dc}=2.25$ V. These weakly pronounced oscillations can occur close to the extrema of the slow envelope oscillations on the θ time scale [see Fig. 2(b)].

For the low to moderate gain conditions presented in Fig. 14(b), the double round trip frequency ν_{P2} appears for nearly

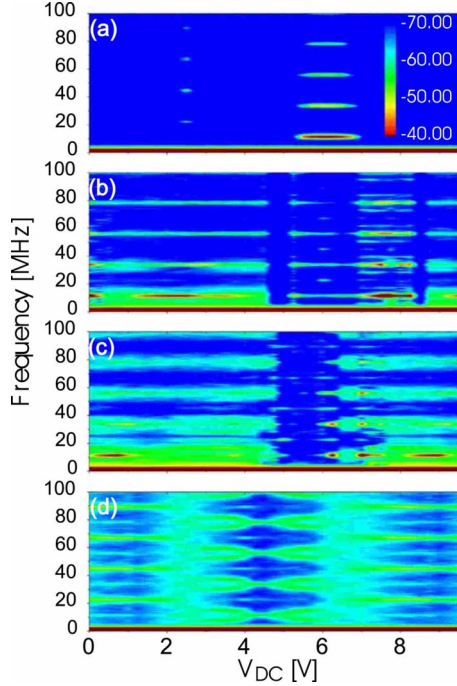


FIG. 14. (Color online) Low-frequency part of the rf spectra of the dynamics in dependence on the MZ bias. The conditions are (a) $I_L=30$ mA, (b) $I_L=45$ mA, (c) $I_L=50$ mA, and (d) $I_L=70$ mA and correspond to a progressively larger gain.

all the Φ values with more or less pronounced weight. The only exceptions are the zero slope regimes of the nonlinearity. It is particularly interesting that the square wave oscillation is present within the fine structure of all the slowly varying envelope time series, found for positive slope of the nonlinearity. Furthermore it can be seen in panel (b) that for the higher harmonic oscillations present at $V_{dc}=6.5$ V [Figs. 7(d) and 9], ν_{p2} and its harmonics do also exist, but with a relatively small amplitude. This is due to the fact that most of the energy is located in the GHz frequency range which is not shown here.

As the feedback gain is further increased, the ν_{p2} signature is more and more diffused, as can be seen in panel (c). This is a consequence of the lower relative weight of the square wave within the breathers envelope. The fine structure of the envelope is mainly chaotic because of the high gain that is available for nearly all the phase space region which is continuously scanned on the slow time scale θ . Only if the envelope dynamics is in vicinity of the zero slope region of the nonlinearity, the local gain is sufficiently small to allow for the square wave oscillations.

Finally, for high feedback gain [panel (d)], the dynamics is strongly nonlinear and chaotic, covering more than one extrema of the nonlinear function with large and fast amplitude fluctuations so that the ν_{p2} signature broadens so much that it disappears. It can still be guessed for Φ values corresponding to low slopes of $f(x)$, but it is nearly absent in the maximum slope region ($V_{dc} \approx 2.5$ or 6.5 V, i.e., $\Phi \approx \pm \pi/4$).

In addition to the high gain chaotic dynamics, we have examined extreme parameter conditions and found two unexpected oscillatory regimes. They are described in detail in the next subsection.

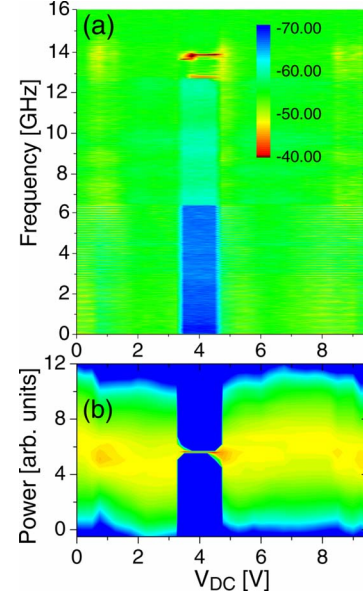


FIG. 15. (Color online) High-frequency range spectral (a) and PDF temporal (b) bifurcation diagram for a high feedback gain of $I_L=75$ mA.

B. High-frequency oscillations

The broad frequency range rf-spectral bifurcation diagram in Fig. 15(a) was obtained for a high gain condition ($I = 75$ mA, or $\beta \approx 4.7$). The expected behavior is a fully developed chaotic regime for the complete available range of the phase parameter space, as reported in Fig. 13. But by contrast to Fig. 13 we now find that a periodic window appears for a Φ range close to the maximum of $f(x)$. As the oscillation frequencies occurs at around 13–14 GHz, with the oscilloscope it is not possible to identify dynamics in the time domain due to the limited bandwidth. This can be seen in the corresponding PDF bifurcation diagram presented in Fig. 15(b). In this representation the high-frequency oscillation appears “virtually” as a stable steady state which corresponds to the mean value of a strictly positive fast oscillation.

According to the model equation (2), the fast oscillation frequency should be related to the high cutoff frequency of the feedback filtering i.e., the inverse of the fast characteristic time τ . To investigate this assumption experimentally, we deliberately modify this high cutoff, setting it to several different values by implementing different standard telecom Bessel-Thomson low-pass filters into the electronic feedback loop. By this we find high-frequency oscillations which turn out to be linearly related to the particular cutoff frequency of the introduced low-pass filters. This interesting result is shown in Fig. 16. We also find that the parameters (β, Φ) for which we find these oscillations, also depend on the imposed cutoff frequency. Decreasing the cutoff frequency of the low-pass filter, the oscillations are observed for lower β , while the phase value continuously increases towards $\Phi = \pi/4$.

Solving Eq. (2) numerically with the experimental values of β and Φ , we did not find the observed fast oscillations. In order to investigate this inconsistency between experiment and modeling, we modified the model taking into account the higher order of the actual differential process. Since the ob-

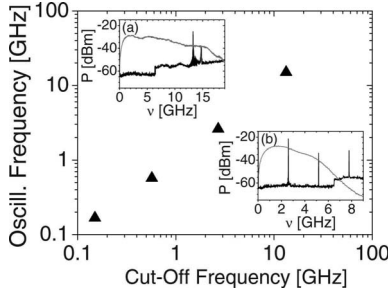


FIG. 16. High-frequency oscillations as a function of the high-frequency cutoff of the bandpass filter. (a) $\nu_{\text{cutoff}}=2.7$ GHz, (b) $\nu_{\text{cutoff}} \approx 12$ GHz. The gray lines in the inset depict the profiles of the corresponding filters.

served properties of the oscillations are obviously determined by the high cutoff properties, we numerically investigated the influence of filtering with a second order high cutoff, while we neglected the low cutoff. This can be done, since the high-frequency oscillations do not give rise to the θ -related low-frequency components in this particular case. With the second order low-pass filter (a filter of Butterworth kind was chosen), we were able to numerically recover the expected fast oscillations with a frequency indeed related to the high cutoff of the filter. The new model equation is given by

$$\tau^2 \frac{d^2x}{dt^2}(t) + \sqrt{2}\tau \frac{dx}{dt}(t) + x(t) = \beta \cos^2[x(t - \tau_D) + \Phi]. \tag{51}$$

The higher order of the high-frequency stop band thus seems to play a major role in the mechanism for this particular rf oscillation. From the numerics, we find that modeling of a second order cutoff can generate these oscillations and the experimentally observed parameter dependence. However, we also find that the tolerable parameter range is smaller than in the experiment which indicates that even higher order filtering might further stabilize this phenomena. The calibrated filters used in the experiment were filters with fifth-order cutoff. Without limiting the feedback bandwidth with those filters (thus using the widest available bandwidth limited by the photodiode, the driver, and the MZ only), the measured cutoff was even of eighth order. Our results suggest that higher order high-pass filtering influences the dynamics when the characteristic time of the slow low-frequency cutoff is of importance. Whether this is indeed the origin of the observed complex single breather envelope dynamics, as discussed in Fig. 10, needs to be further investigated.

C. Multipulse dynamics

Finally, we report on another very different behavior observed in our system, which might be related to multipulse excitability. This phenomenon has been theoretically predicted for an optically injected semiconductor laser [26]. Recently multipulse excitability has also been observed experimentally [27,28]. In our setup, a particular pulse behavior with similar properties is observed for moderate feedback,

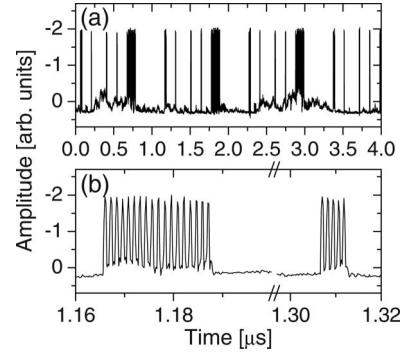


FIG. 17. Multipulse dynamics for $\tau_D=1.1 \mu\text{s}$.

and Φ around the maximum of the nonlinear function $f(x)$. However, a significant parameter change is proposed with respect to the previously reported dynamical regimes. Specifically, the delay τ_D is set to the larger value of $1.1 \mu\text{s}$.

For these conditions we can find pulsating dynamics. An example is presented in Fig. 17 in which panel (a) shows a $4 \mu\text{s}$ long segment of the amplitude time series measured with an ac detector, while a zoom into the time series is depicted in (b). The time series show that the dynamics is repetitive on different time scales. Specifically, we find sequences of regularly spaced pulse package with a repetition rate of the order of 1 GHz. The number of pulses within each package can vary considerably, as it can be seen in (b). However, the global pattern of pulse package sequences is repetitive (almost periodic) with a period of twice the delay. Interestingly, the mean number of pulse packages, as well as the number of pulses in each package strongly depends on Φ and β . We find that parameter variations of the order of a few percent also can lead to irregularly distributed pulse sequences for which we cannot identify a global $2\tau_D$ -repetitive pattern. Increasing further β or varying Φ , the dynamics typically evolve into a chaotic regime, in which the dynamics become broadband, comprising the full dynamical bandwidth of the system.

The mechanism leading to this kind of self-pulsating behavior in our delay system is still being investigated. One difficulty is the need for long simulations due to the large delay time resulting in very long transients. A second difficulty is the possibility that higher order filtering effects as in previously analyzed high gain case cannot be neglected. This has motivated new asymptotic studies which are currently in progress. Nevertheless, work is in progress to support understanding of this, as well as the other unusual behaviors that have been observed in this broadband band-limited nonlinear delayed feedback oscillator, with analytical derivations.

VII. DISCUSSION AND CONCLUSION

We have investigated the dynamical properties of an optical oscillator subject to a delayed bandpass filtering feedback. Its dynamical response is described by an integro-DDE that differs from Ikeda family of first-order DDEs, only by the presence of an integral term. Depending on the feedback phase, two different routes to limit-cycle oscillations have been explored both experimentally and analytically. Our re-

sults are interesting on three different levels. First, the presence of different time scales in the problem does not immediately lead to a multiperiodic or chaotic regimes. For relatively low feedback rate, a fast square-wave and a low-frequency time-periodic regime have been observed. Practically, the classical square-wave output caused by a large delay is no more the only possible waveform. Second, new bifurcation mechanisms have been identified that are responsible for the progressive modifications of the basic time-periodic solution. Third, the mathematical limit from the iDDE to the DDE as the high-pass filter time response goes to infinity (or its frequency cutoff goes to zero) is highly singular and each case needs to be carefully explored.

For increased feedback gains, these typical iDDE periodic oscillations have been found to bifurcate through different mechanisms, depending essentially on Φ . The integral time scale slow periodic regime evolves into complex periodic and chaotic breathers. They are consisting of fast bursting oscillations with the differential time scale τ and θ , as well as the delay time scale τ_D . These breathers show slowly varying amplitudes, superimposed to a slow periodic envelope of the order of the integral time scale.

The square wave periodic oscillation ruled by the delay, bifurcates into faster nearly square waveforms, which have shown a higher harmonic resonance with the very fast differential time scale. For high feedback gains, the two distinct dynamical regimes finally merge all into broadband chaotic oscillations, for any value of the parameter Φ . These oscillations are covering the whole bandwidth of the oscillator, revealing complex nonlinear mixing of the three different time scales that were separately dominating at low feedback gains: the slow integral time scale, the delay, and the fast differential time scale.

Additional particular behaviors have been also reported that correspond to extreme physical parameter settings: high-frequency locking at strong feedback gains, or pulsating behavior with complex pulse patterns for very large delays. The described dynamical behaviors are far from being exhaustive considering the huge range of possible parameter settings for our setup. In addition to further explore the possible dynamical outputs of our system, theoretical, numerical, and analytical work is required to better understand the different mechanisms. Many of the new dynamical features, such as, e.g., the occurrence of very low-frequency oscillation related to the low-frequency cutoff time and the breathers dynamics, are already captured by the model we have derived in Eq. (2). This demonstrates that an integrodifferential process (and also higher-order filtering) can lead to different dynamical phenomena than the ones known for the commonly considered standard differential processes. Such effects may also arise in other information transmission systems in modern communication technologies, or in living systems in the fields of neurobiology. Furthermore, integrodifferential processes are widely spread in many control engineering applications using the proportional integral derivative (PID) control system described by the same linear terms in Eq. (2). Delay effects are being intensively investigated in control theory [29], since they are concerned. However, they usually do not consider strong or moderate nonlinearities, which might induce important instability phenomena as the numerous ones described in this article.

ACKNOWLEDGMENTS

This work was mainly conducted in the frame of the European PICASSO project (Grant No. FP6-2006-IST-2.5.1) and partly within the french national project ACSCOM. The authors thank the Region Franche-Comté and the CNRS for their support of advanced optical telecommunication research program within the FEMTO-ST institute. L.L. is thankful for the support of the “Institut universitaire de France.” T.E. acknowledges the support of the Fonds National de la Recherche Scientifique (Belgium).

APPENDIX

1. Numerical integration scheme

Numerical simulations reported in Figs. 2(b) and 11(c) were obtained after integrating numerically the normalized two variable differential delay equation (5) [obtained from the integrodifferential model (2)], with a standard fourth-order Runge-Kutta algorithm adapted for delay equations. With such a delay dynamics, the integration procedure requires a permanent memory of the last computed samples over a time interval corresponding to the delay, thus constituting a complete initial condition for the dynamics, or differently speaking, a full state of the infinite dimensional phase space. Then, the most important numerical problems encountered with this kind of huge multiple time delay dynamical system, are the long computation time required to construct a transient free τ_D initial condition [typically a few thousands of τ_D -long time intervals as for the solution in Fig. 11(b)] and a very long waveform that is able to cover both the very fast fluctuations of the order of τ , as well as the very slow envelope related to θ .

The first issue concerns only the computation time, without any technical problem. The second issue is, however, strongly concerned by memory overflows, if one would like to keep all the samples for the whole duration of a very slow envelope as in Fig. 11(b). This has been experienced as not possible with “standard” up-to-date PCs, even with 2 Gb RAM memory. The represented waveform in Fig. 11(b) was calculated using small gathered time slots, each of which was individually obtained with the full integration time step resolution, but then filtered and undersampled to keep a reasonable memory for the representation of the full envelope.

Quantitative informations about the calculation of the breather waveform in Fig. 11(b) are as follows: integration time normalized to the fast characteristic time τ was $h=0.02$, the number of samples required to consider the actual experimental delay τ_D reported in Table I is then 3.43×10^3 , which represents a dynamics memory, or a dimension of the numerical integration, of around 170k samples, and the ratio $\varepsilon=\tau/\theta$ indicating the full time scale spreading of nearly 6 orders of magnitude was 2.45×10^{-6} .

The long breather envelope would thus require a full resolution representation of around 0.2G samples with a double real amplitude representation: this is far beyond the limit for memory overflow with the available computation means. To manage this memory overflow problem, we calculated 10

times a $50 \tau_D$ -long time series, each of which was filtered and undersampled with a factor 400. After combining these 10 filtered time series, the resulting 500 τ_D -long waveform could thus cover the whole breather envelope duration, as represented in Fig. 11(b). The choice of this 400 undersampling factor was also motivated by the actual experimental number of samples, so that the numerically obtained time series had also the same number of samples. Both numerical and experimental time series were then processed in a easily comparable way through a wavelet transform.

2. The wavelet analysis

To look for characteristic frequencies within the temporal envelop, we used the continuous wavelet transforms [30] in Fig. 11, in order to unfold time series into time and frequency. The wavelet transform $W_x(a, t)$ of a signal $x(t)$ is defined as

$$W_x(a, t) = \int_{-\infty}^{+\infty} \Psi_a(t - \tau)x(\tau)d\tau, \quad (\text{A1})$$

where the function $\Psi_a(t)$ originates from the Morlet mother wavelet $\Psi(t)$, and the scaling parameter a :

$$\Psi_a(t) = \frac{1}{\sqrt{a}}\Psi\left(\frac{t}{a}\right) = \frac{1}{\sqrt{a}}e^{-(1/2)(t/a)^2}e^{j\omega_0(t/a)}. \quad (\text{A2})$$

The scale parameter a allows to expand or contract the wavelet before convoluting it with the signal. The wavelet acts as a filter, by selecting the components of $x(t)$ that correspond to the frequencies centered at $f = \omega_0/a$ [ω_0 is typically set to 5.5, thus leading to the vertical scale in Figs. 11(c) and 11(d)]. The coefficient $W_x(a, t)$ assumes a high value when there is a significant contribution of the signal at the frequency f and at the time t . The advantage with respect to the usual Fourier transform lies in a local spectral analysis in time instead of a global one.

-
- [1] G. Stépán, *Retarded Dynamical System: Stability and Characteristic Functions* (Longman, London, 1989).
- [2] A. Beuter, L. Glass, M. Mackey, and M. Titcombe, *Nonlinear Dynamics in Physiology and Medicine* (Springer-Verlag, New York, 2003).
- [3] C. P. Fall, E. S. Marland, J. M. Wagner, and J. J. Tyson, *Computational Cell Biology* (Springer-Verlag, New York, 2002).
- [4] D. Kane and A. Shore, *Unlocking Dynamical Diversity: Optical Feedback Effects on Semiconductor Lasers* (Wiley, London, 2005).
- [5] J.-P. Goedgebuer, P. Levy, L. Larger, C.-C. Chen, and W. T. Rhodes, *IEEE J. Quantum Electron.* **38**, 1178 (2002).
- [6] N. Gastaud, S. Poinot, L. Larger, M. Hanna, J.-M. Merolla, J.-P. Goedgebuer, and F. Malassenet, *Electron. Eng. (U.K.)* **40**, 898 (2004).
- [7] A. Argyris, D. Syvridis, L. Larger, V. Annovazzi-Lodi, P. Colet, I. Fischer, J. Garcia-Ojalvo, C. R. Mirasso, L. Pesquera, and A. K. Shore, *Nature (London)* **438**, 343 (2005).
- [8] C. P. Fall, E. S. Marland, J. M. Wagner, and J. J. Tyson, *Mathematical Models of Hematopoietic Cell Replication and Control*, edited by H. G. Othmer, F. R. Adler, M. A. Lewis, and J. C. Dallon (Prentice Hall, New York, 1997), 149–178.
- [9] K. Ikeda, H. Daido, and O. Akimoto, *Phys. Rev. Lett.* **45**, 709 (1980).
- [10] M. Schanz and A. Pelster, *Phys. Rev. E* **67**, 056205 (2003).
- [11] H. M. Gibbs, F. A. Hopf, D. L. Kaplan, and R. L. Shoemaker, *Phys. Rev. Lett.* **46**, 474 (1981).
- [12] A. Neyer and E. Voges, *IEEE J. Quantum Electron.* **18**, 2009 (1982).
- [13] T. Aida and P. Davis, *IEEE J. Quantum Electron.* **28**, 686 (1992).
- [14] V. S. Udaltsov, L. Larger, J.-P. Goedgebuer, M. W. Lee, E. Genin, and W. T. Rhodes, *IEEE Trans. Circuits Syst., II: Analog Digital Signal Process.* **49**, 1006 (2002).
- [15] L. Illing and D. J. Gauthier, *Physica D* **210**, 180 (2005).
- [16] Y. C. Kouomou, P. Colet, L. Larger, and N. Gastaud, *Phys. Rev. Lett.* **95**, 203903 (2005).
- [17] The integrodifferential equation is equivalent to a second order differential equation that reduces to a first-order one in the limit θ large.
- [18] L. Larger, J.-P. Goedgebuer, and J.-M. Merolla, *IEEE J. Quantum Electron.* **34**, 594 (1998).
- [19] K. Ikeda and K. Matsumoto, *Physica D* **29**, 223 (1987).
- [20] Y. K. Chembo, L. Larger, H. Tavernier, R. Bendoula, E. Rubiola, and P. Colet, *Opt. Lett.* **32**, 2572 (2007).
- [21] K. Ikeda, K. Kondo, and O. Akimoto, *Phys. Rev. Lett.* **49**, 1467 (1982).
- [22] A. Neyer and V. E. Voges, *Opt. Commun.* **37**, 169 (1981).
- [23] X. S. Yao and L. Maleki, *Electron. Lett.* **30**, 1525 (1994).
- [24] B. Dorizzi, B. Grammaticos, M. Le Berre, Y. Pomeau, É. Res-sayre, and A. Tallet, *Phys. Rev. A* **35**, 328 (1987).
- [25] Y. C. Kouomou, P. Colet, L. Larger, and N. Gastaud, *IEEE J. Quantum Electron.* **41**, 156 (2005).
- [26] S. Wiczczonek, B. Krauskopf, and D. Lenstra, *Phys. Rev. Lett.* **88**, 063901 (2002).
- [27] D. Goulding, S. P. Hegarty, O. Rasskazov, S. Melnik, M. Hartnett, G. Greene, J. G. McInerney, D. Rachinskii, and G. Huyet, *Phys. Rev. Lett.* **98**, 153903 (2007).
- [28] O. Vaudel, Ph.D. thesis, University of Rennes, France, 2007.
- [29] J.-P. Richard, *Automatica* **39**, 1667 (2003).
- [30] I. Daubechies, *SIAM J. Appl. Math.* **61**, 194 (1994).